CEAS Aeronautical Journal
https://doi.org/10.1007/s13272-025-00856-9

ORIGINAL PAPER

Transition prediction including turbulent wedges for a forward swept natural laminar flow wing

Michael Fehrs[1] · **Christoph Kaiser**[1]

Received: 10 September 2024 / Revised: 28 April 2025 / Accepted: 20 May 2025

Abstract
In the LuFo VI/2 project ULTIMATE, a forward swept natural laminar flow wing is tested in the European transonic wind tunnel. The high Mach and high Reynolds number wind tunnel test is intended to provide necessary data for transition model validation. This article gives an overview of the wind tunnel test and the associated validation activities for the DLR γ transition model. The accuracy in the prediction of aerodynamic forces in a transitional flow is shown for rigid and coupled CFD–CSM computations. For the coupled computations, the effect of turbulent wedges on the aerodynamic predictions is shown. Although turbulent wedges are often disregarded as a mere side effect of high Reynolds number wind tunnel testing, it is found that these wedges are important for the understanding of the overall aerodynamics of the wind tunnel configuration.

Keywords Transition model validation · Local correlation-based transition model · Turbulent wedges · CFD–CSM computation

1 Introduction

Today's ecological and economical constraints require the development of more efficient transport aircraft designs, e.g., by reducing the overall aircraft drag. One way to achieve this is the application of laminar flow technology (active, passive, and hybrid). In the LuFo[1] VI/2 project ULTIMATE,[2] a forward swept laminar wing configuration named NLF-ECOWING-FSW is tested in the European Transonic Wind tunnel (ETW) [1]. The wing-fuselage wind tunnel half model is based on the TuLam short/medium-range aircraft configuration [2]. The forward sweep (FSW) of the natural laminar flow (NLF) wing allows for a smaller leading edge sweep compared to a backward swept wing albeit having the same semi-chord sweep angle. A reduced leading edge sweep angle attenuates the occurrence of crossflow transition and a large semi-chord sweep is important to reduce detrimental compressibility effects in transonic flow [2].

The goal of the steady wind tunnel test is to assess the performance of the overall wing/fuselage design at realistic Mach and Reynolds numbers and to provide validation data for computational fluid dynamics (CFD) transition prediction methods. These data are of utmost importance for the validation of correlation-based transition models as most experimental data used for calibration and validation are located in the low Reynolds number range. A consecutive unsteady wind tunnel test in a later wind tunnel campaign will provide data for the validation of the predictive capabilities of correlation-based transition models for unsteady boundary-layer transition on a pitching wing.

Davies et al. [3] performed preliminary coupled CFD–CSM[3] computations with a simplified structural model of the NLF-ECOWING-FSW. Based on these investigations, the jig shape of the wing is developed. The jig shape of the wing is the shape that occurs with no aerodynamic loading acting on the wing. Under the design loading, the jig shape deforms into the design shape. A first set of computations to be directly compared to the wind tunnel data is performed by Helm et al. [4] based on the design shape of the wing. For these computations, the TAU transition module [5, 6]

✉ Michael Fehrs
michael.fehrs@dlr.de

Christoph Kaiser
christoph.kaiser@dlr.de

[1] Institute of Aeroelasticity, DLR, Bunsenstr. 10,
37073 Göttingen, Germany

---

[1] Luftfahrtforschung.

[2] Ultra high efficient wing and moveables for next generation aircraft.

[3] Computational Fluid Dynamics-Computational Structural Mechanics.

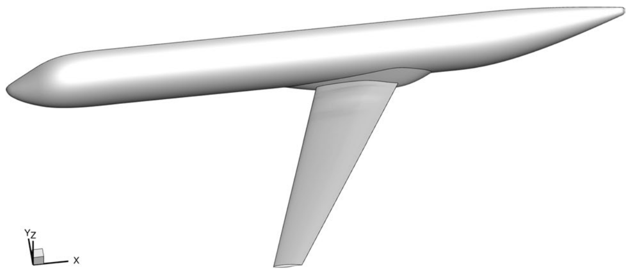

Fig. 1 CAD model of the NLF-ECOWING-FSW wind tunnel configuration

is used, which employs an e^N method [7, 8]. The computations show a large extent of laminar flow in agreement with the wind tunnel data. The experimental transition location is determined based on temperature-sensitive paint (TSP) measurements [9].

At high Reynolds numbers, turbulent wedges occur in the laminar boundary layer easily due to contamination or surface imperfections. Helm et al. [10] show the effect of turbulent wedges on the aerodynamics of the NASA CRM-NLF configuration[4] at high Reynolds numbers. These computations are based on the TAU transition module, which allows the prescription of a fixed transition location. In the present investigation, the DLR γ transition model [11] is used for transition prediction. A newly developed method to include turbulent wedges for intermittency-based transition models [12] is applied to account for turbulent wedges detected in the wind tunnel test by the TSP measurements. The aerodynamic predictions are strongly improved once the turbulent wedges are included in the numerical computations.

This article will give a detailed description of the numerical activities to further validate the DLR γ transition model for transonic high Reynolds number flows based on the ETW test data. The next section will describe the experimental test conditions and the numerical set-up. This includes a description of the solver and solver settings, the steady coupling procedure, the finite-element model, CFD grids, the wind tunnel model, and measurement techniques. The third section will present the numerical results in comparison to the experimental data. The last section will conclude this article.

2 Methods and set-up

2.1 NLF-ECOWING-FSW configuration

Figure 1 shows the computer-aided design (CAD) model of the NLF-ECOWING-FSW wind tunnel configuration. The baseline short/medium-range aircraft configuration with a leading edge sweep angle of $\phi_{\mathrm{LE}} = -17°$ is designed for a cruise Mach number of $M = 0.78$ at a flight level FL = 350 with a design lift coefficient of $C_{\mathrm{L}} = 0.52$. The airfoil design allows for laminar boundary-layer flow up to the shock location [2].

The wind tunnel model is scaled by 1/13.6 compared to the baseline aircraft configuration. For all non-dimensional aerodynamic data, a reference wing area of $S_{\mathrm{ref}} = 0.3298\,\mathrm{m}^2$ and a reference length of $c_{\mathrm{ref}} = 0.28647\,\mathrm{m}$ are used. The moment reference center of the wind tunnel model is located at the quarter chord location of the wing root at $(x, y, z) = (1.318881\,\mathrm{m},\ 0.0\,\mathrm{m},\ 0.0\,\mathrm{m})$. In the wind tunnel, the model is mounted on a peniche with a height of 0.04 m. The peniche as well as the wind tunnel walls are not accounted for in the computations.

2.2 CFD solver and flow models

The DLR TAU-Code [13] is used in this investigation with the DLR γ transition model [11] in combination with the SST k-ω turbulence model [14] for transition prediction. Fully turbulent computations are based on the SST k-ω turbulence model alone. For these fully turbulent computations, the turbulence model is active in the whole flow field without considering any laminar boundary-layer flow, e.g., upstream of the experimental tripping locations. For both types of flow, the SST k-ω turbulence model is augmented by employing the quadratic constitutive relation (QCR) [15] and the SST rotation correction (SSTRC) [16]. The effects of these augmentations on the turbulent and transitional flows are described in more detail in the results section.

A central scheme with artificial matrix dissipation [17] is used for the convective flux discretization of the mean flow equations in all computations. The convective fluxes of the turbulence equations are discretized with a second-order Roe upwind scheme. A local time step is used in combination with an implicit Backward–Euler scheme in the steady computations to accelerate convergence employing an LU-SGS scheme [18].

Intermittency transport models like the γ transition model [19] or the DLR γ transition model [11] show a high sensitivity to local disturbances in high Reynolds number flows. A slight increase in intermittency can lead to an abrupt transition to a turbulent boundary-layer state. This behavior is exploited to create a local boundary-layer tripping by forcing intermittency values of $\gamma = 1$ at turbulent wedge apices or at a boundary-layer tripping location. In a pre-processing step, the location of a turbulent wedge apex and a disturbance radius are defined and grid points within the disturbance radius are identified. Based on the grid point ID, these nodes are assigned an intermittency value of $\gamma = 1$ throughout the whole computation. For spherical disturbances at the wedge

---

[4] Common Research Model with Natural Laminar Flow wing.

apex, a turbulent wedge forms due to the advection and diffusion characteristics of the γ transport equation. Fehrs [12] gives a complete description of the method with a discussion of effects like disturbance size, grid resolution, and diffusion parameters for the NASA CRM-NLF configuration at similar Mach and Reynolds numbers as investigated in this study.

This method to include turbulent wedges is an ad-hoc solution to model the effect of known turbulent wedges on the boundary-layer flow. The high sensitivity of the DLR γ transition model in combination with the SST k-ω turbulence model is in general not desirable as the model might give different results for different initial conditions (e.g., starting from a fully laminar or fully turbulent boundary-layer state). François and Krumbein [20] reduced this sensitivity of the DLR γ transition model for the coupling with the SA-neg model. The direct approach by forcing intermittency values of $\gamma = 1$ might not be suited for such a less-sensitive implementation of an intermittency transport model and a more complex approach might be needed (e.g., by modifying the source terms of the transition model).

2.3 Grid generation

Centaur™ V16.0 by CentaurSoft [21] is used to build the CFD grids for the design and jig shape of the NLF-ECOWING-FSW. The hybrid grids consist of a structured quadrilateral surface mesh on the wing with 300 grid points in chord and spanwise direction, an unstructured triangular mesh on the wing tip and fuselage, and an unstructured quadrilateral surface mesh on the belly fairing. At the leading and trailing edge of the wing, the chordwise non-dimensional grid spacing in terms of local chord length is about $\Delta x/c_{\text{local}} \approx 10^{-3}$ with a chordwise growth rate of 1.1 resulting in a grid spacing of $\Delta x/c_{\text{local}} \approx 3.6 \cdot 10^{-3}$ on the wing surface. The blunt trailing edge is meshed with a structured quadrilateral surface mesh as well. Five equidistant grid points are placed over the height of the trailing edge.

Hexahedral and prismatic boundary-layer grids with nominally 75 layers are created upon the respective quadrilateral and triangular surface meshes. The first layer height is approximately $1.84 \cdot 10^{-7}$ m and results in a total stack height of ≈ 0.0188 m for a wall-normal growth rate of 1.1. The first cell height results in $y^+_{\text{max}} < 1$ for all computations presented. On the fuselage and belly fairing, a nominal value of 85 layer is used to account for the larger boundary-layer thickness.

Figure 2 shows the boundary-layer grid and the intermittency distribution at the transition onset location. The non-dimensional chordwise grid spacing is $\Delta x/c_{\text{local}} \approx 3.6 \cdot 10^{-3}$. The first intermittency increase in the boundary layer occurs within the structured hexahedral grid. The intermittency increase in streamwise direction does not occur abruptly over the full height of the boundary layer but develops over the length of some grid cells. This is the desired behavior for an intermittency transport model [19].

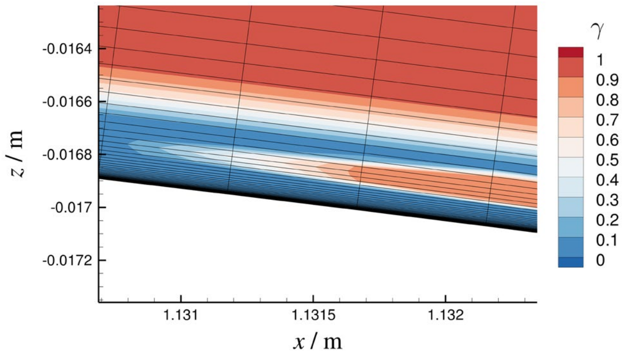

Fig. 2 Boundary-layer grid and intermittency distribution in the transition region with a non-dimensional chordwise grid spacing of $\Delta x/c_{\text{local}} \approx 3.6 \cdot 10^{-3}$

Figure 3 shows the surface mesh at the leading edge of the wing root (left) and the outer faces of the boundary-layer mesh (right). At the wing-fuselage intersection, the number of boundary-layer cells is reduced automatically once stack collisions occur. Only in this region at the intersection between the boundary layer and tetrahedral grid, single cells with higher skewness are created.

The remaining flow field is meshed with tetrahedral elements growing in size towards the far field. The hemispherical far-field boundary is approximately 30 wing semi-spans away from model ($b/2 = 1.25$ m). The grid generation settings for the jig and design shape are identical. The overall meshes consist of approximately $37 \cdot 10^6$ elements with $19.5 \cdot 10^6$ grid points. The surface girds consist of 253,000 surface quadrilaterals and 87,000 surface triangles.

A complete grid convergence study is beyond the scope of this investigation, but grid parameters like the chord and spanwise grid spacing have been varied to exclude grid effects. In addition, the previous investigations on this configuration are taken into account for the grid generation [3, 4]. For the turbulent wedge method, Fehrs [12] performed an extensive grid study for similar flow conditions, which results are considered in this investigation as well.

2.4 FE solver and structural model

The coupled CFD–CSM computations require a modal description of the structural model with its (mass scaled) eigenmodes and eigenfrequencies. ANSYS® Mechanical Enterprise, Release 2022 R2 [22] is used to perform the structural modal analysis. As the full CAD model is too detailed for an analysis, the model complexity is reduced by selecting only certain model components for the FE analysis. In addition, a certain amount of defeaturing is

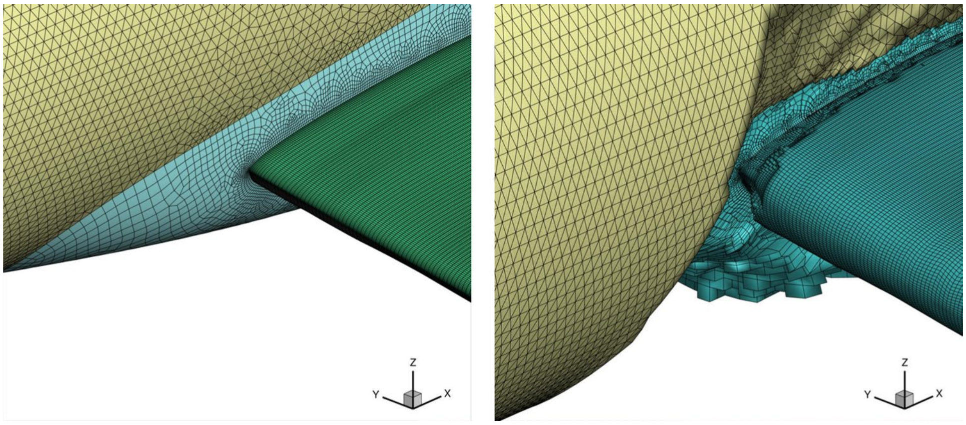

Fig. 3 Left: surface grid at the leading edge of the wing root. Right: outer faces of the boundary-layer grid. Due to stack collisions, the number of boundary-layer cells is reduced at the wing–fuselage intersection

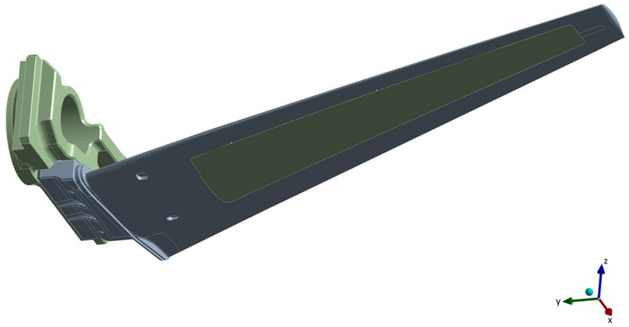

Fig. 4 CAD assembly of the NLF-ECOWING-FSW consisting of wing, adapter, and main cover plate on the lower wing surface shown here in different colors

performed on these components using ANSYS® DesignModeler, Release 2022 R2 [23].

Figure 4 shows the CAD assembly of the NLF-ECOWING-FSW as it is used in the FE analysis. The model consists of the main wing, the wing adapter, and the cover plate on the lower surface. The CAD geometry represents the jig shape with no aerodynamic or gravitational loading. The adapter connects the wing with the fuselage and the wind tunnel support. There are two compartments beneath the cover plate that allow access to the measurement equipment integrated into the wing. Details like pressure sensor ducts are disregarded to reduce the overall model complexity.

For all parts of the model, a maraging steel with Young's modulus $E = 2 \cdot 10^{11}\,\mathrm{N/m^2}$, Poisson's ratio of $\nu = 0.266$, and density $\rho = 7920\,\mathrm{kg/m^3}$ is applied. The cover plate is connected to the wing by 38 bolts. The wing itself is connected with 10 bolts to the adapter. To represent these bolted connections with a minimum of complexity, a circular face of the size of the threaded hole is created for each bolt. These faces are then used as bonded contacts (no separation, no slip) in the FE model [24]. The connections of the adapter to the fuselage and to the wind tunnel support are modeled as a fixed support applied on the respective faces with no representation of any connecting bolts.

A patch conforming method [24] is used to create a tetrahedral mesh with quadratic element order. The overall mesh consists of 292,757 elements with 514,389 nodes. In the modal analysis, only the first six modes are identified as it is expected that the large model stiffness will reduce the influence of higher modes strongly. These six modes represented by their eigenvectors and eigenfrequencies are used in the static CFD–CSM coupling.

2.5 Static CFD–CSM coupling

Although the wind tunnel model is rather stiff and preliminary investigations showed only small deformations [3], a difference in the local angle of incidence can have an effect on the transition location due to changes in the streamwise pressure gradient. To account for the deformation of the wind tunnel model under wind loading, static coupled CFD-CSM computations are performed within the FlowSimulator [25] environment. The static coupling is based on the aerodynamic surface model of the jig shape and the structural model described above. The gravitational force is disregarded as the model is mounted on the wind tunnel ceiling with the wing tip pointing downwards.

Broyden's method [26] is used to obtain the static aeroelastic equilibrium in an iterative procedure starting at a steady CFD solution. The method is based on modal coordinates and the mode shapes are interpolated on the CFD grid by a thin-plate spline method [27] in a pre-processing step. The aerodynamic forces computed by the CFD solver are projected onto the mode shapes to obtain the generalized forces for each mode at each iteration step. The modal displacements are found by the quasi-Newton step of Broyden's method and the surface grid is deformed accordingly. The deformation of the surface grid is propagated into the volume mesh by radial basis functions [28]. For each static coupling computation, a total of 20 iterations are performed.

Figure 5 shows an example for the residual between the structural and aerodynamic forces on the left and the modal displacements for the first three modes on the right for a transitional flow. The residual is given by the Frobenius norm of the residual vector of all modes normalized by the residual of the first iteration. The modal displacements are normalized by the displacement of the last iteration for each mode. Although the residual is not monotonically decreasing over the full solver run, the modal displacements are settled after approximately the first five iterations.

2.6 Wind tunnel test and data

The performance test in the ETW is conducted at Mach numbers in the range of $M = 0.20$ to 0.82 for Reynolds numbers between $Re = 6 \cdot 10^6$ and $18 \cdot 10^6$. Most data are acquired at the design Mach number of $M = 0.78$ at a Reynolds number of $Re = 16 \cdot 10^6$. The working fluid in the ETW is nitrogen. The combination of high Reynolds and high Mach number is achieved by cryogenic temperatures and moderately high pressures. [1]

Free boundary-layer transition is only desired on the upper wing surface. At the fuselage nose and at the leading edge of the lower wing surface, transition trippings are applied through transition bands with ballotinis (small glass balls in an adhesive). These transition bands are located on the fuselage 0.045 m downstream of the tip of the nose and on the lower surface at 5% local chord length. For the fully turbulent tests, a transition band is added on the upper wing surface at 5% local chord length. [1]

The complete wind tunnel model is connected to the ETW half model balance to provide the aerodynamic forces (excluding side forces). Aerodynamic forces are made available in terms of non-dimensional aerodynamic coefficients directly comparable to CFD data.

The wing is equipped with 62 static pressure sensors on an inboard wing section at the 13.6% span location. These pressure sensors are distributed along the upper and lower wing surface (row A). In addition, 61 unsteady pressure transducers are located in three measurement rows (B, C, and D) on the upper surface. These pressure transducers are staggered to avoid measurements in turbulent flow emerging from upstream located sensors. Figure 6 shows the wing planform and the location of the pressure rows A to D. In addition, the outer edges of the TSP pockets are shown. These four TSP measurement fields are integrated in the upper surface to detect the transition location. A temperature step method, heating based on carbon nanotubes, and heating through an infra-red laser technique are tested to generate the required temperature change to acquire TSP images [29].

The model deformation is measured through a stereo pattern tracking (SPT) system using markers on the lower wing surface. The SPT data are processed by ETW to describe the bending relative to the sectional semi-chord and the sectional twist angle. It should be noted that SPT and TSP data are not available for the same measurement points. In addition, the wing is equipped with ten accelerometers. These

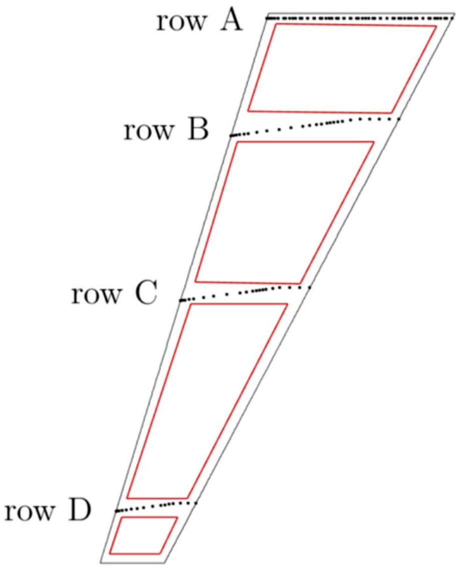

Fig. 6 Wing planform with pressure rows (black dots) and TSP pockets (red lines) on the upper surface

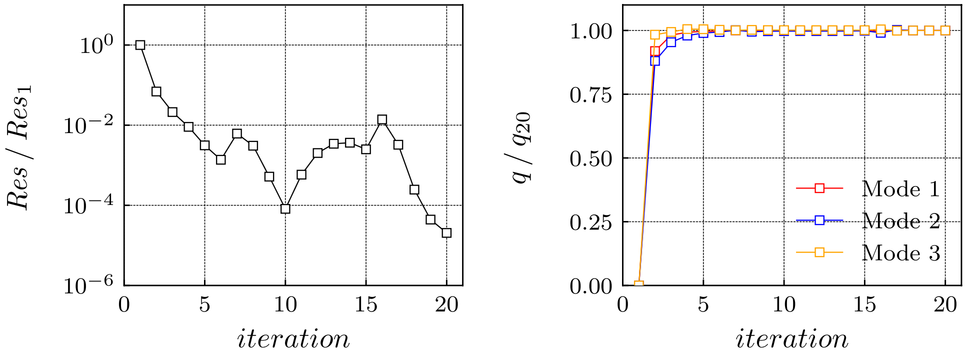

Fig. 5 CFD-CSM solver residual and modal deformation of mode 1–3 at $\alpha = 1°$, $M = 0.78$, $Re = 16 \cdot 10^6$ in a transitional flow

accelerometers are used for real-time monitoring of vibration levels and provide structural data for the validation of the numerical wind tunnel set-up.

3 Results

3.1 Structural model

The experimental and numerical eigenfrequencies of the first six eigenmodes are given in Table 1. The numerical model gives a fair representation of the wind tunnel model. It is not possible to assess all computed modes as the orientation of the accelerometers allows only the identification of out-of-plane components. The third mode is dominated by an in-plane motion with some torsional participation. Especially, this in-plane mode and the 1st torsion mode are influenced by the way the connection between the wing and cover plate is modeled. As the whole model is made of maraging steel and only minor defeaturing is applied, it is assumed that the mass distribution of the structural model gives a good representation of the actual wind tunnel model.

Table 1 Experimental and numerical mode shapes and eigenfrequencies

No	Description	Num. frequency (Hz)	Exp. frequency (Hz)	Err (%)
1	1st bending	30.38	29.0	+ 4.76
2	2nd bending	105.85	99.0	+ 6.92
3	1st in-plane	176.27		
4	3rd bending	232.11		
5	1st torsion	274.79	283.7	− 3.14
6	4th bending	384.28		

3.2 Fully turbulent computations

As a precursor to transitional computations, fully turbulent computations are performed to determine specific parameter settings for the underlying turbulence model at a Reynolds number of $Re = 16 \cdot 10^6$ and a Mach number of $M = 0.78$. For the jig shape computations and the subsequent coupled computations, a N_2 gas model is used. The computational flow conditions are specified by setting the experimental static temperature and pressure at the nominal Mach number of $M = 0.78$ to obtain the right aerodynamic loading. These settings result in a dynamic pressure of $q_\infty = 34\,762$ Pa compared to 34, 820 Pa in the experiment. The flow conditions for the rigid design shape computations are specified by the nominal Mach and Reynolds number directly.

No transition tripping is applied and the whole boundary-layer flow on all parts of the model is treated as fully turbulent. A significant effect on the aerodynamics is found by employing the quadratic constitutive relation (QCR) [15] and the SST rotation correction (SSTRC) [16].

Figure 7 shows the lift and moment coefficients in the full experimental angle of attack range. The computations are performed with QCR and SSTRC for the design, jig shape, and coupled CFD–CSM computations. The coupled computations agree well with the experimental data up to an angle of attack of $\alpha = 2°$. The solver does not converge for $\alpha > 2°$ to a steady solution and error bars are included to show the maximum deviation from the mean.

For these angles of attack, a strong shock develops inboards on the upper wing surface leading to a shock-induced separation at the shock foot. In addition, a small boundary-layer separation develops on the wing–fuselage intersection at mid chord, where the shock on the upper wing impinges on the fuselage. As the angle of attack increases,

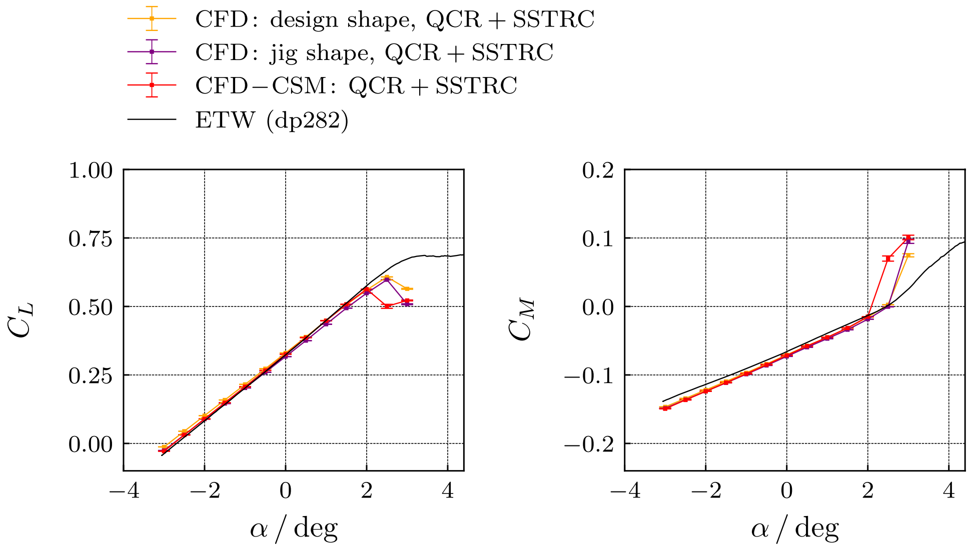

Fig. 7 Turbulent lift and moment coefficient curves in the full experimental angle of attack range with QCR and SSTRC

both effects combine forming a massive separation. This effect is not observed in the experiment.

Figures 8 and 9 show a detail view of the lift and moment curves for the computations with and without QCR and SSTRC, respectively. The agreement between experiment and design shape and the coupled computations is best with the QCR and SSTRC extension. The lift coefficient is in better agreement with the experimental data than the moment coefficient for all computations.

Figure 10 shows the pressure coefficient distributions for both computational settings with and without QCR and SSTRC and the experimental data. The CFD data are only evaluated at the experimental pressure sensor locations. The overall agreement of the coupled CFD–CSM computations with the experiment is good for both settings, especially in sections B–D. For section A, the model extensions improve the predicted first shock position. In addition, the pressure distribution on the aft section of the lower surface is in better agreement employing QCR and SSTRC.

Figure 11 shows the experimental and computational wing bending and twist distributions. The computations give a good representation of the wing bending for a similar aerodynamic loading in terms of C_L. The wing twist is not met exactly, but the differences between experimental and numerical data at the wing tip are only about $\Delta r_y \approx 2.6 \cdot 10^{-2}$ deg. The effect of the different numerical settings on the wing deformation is negligible.

3.3 Transitional computations

Computations with free boundary-layer transition on the upper wing surface are performed at $Re = 16 \cdot 10^6$ and a Mach number of $M = 0.78$ for a turbulence level of $Tu = 0.1$ %. The flow state for the different computations

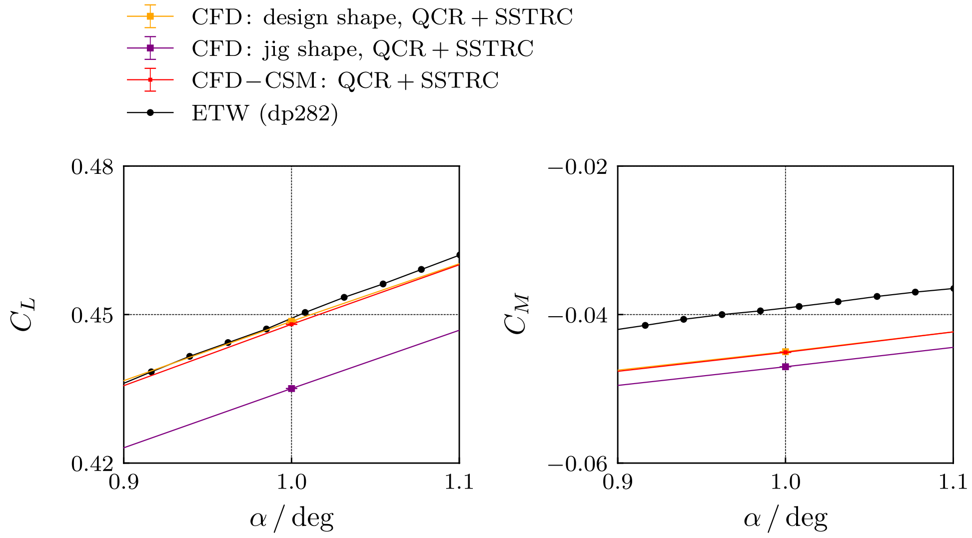

Fig. 8 Detail view of turbulent lift and moment coefficients with QCR and SSTRC

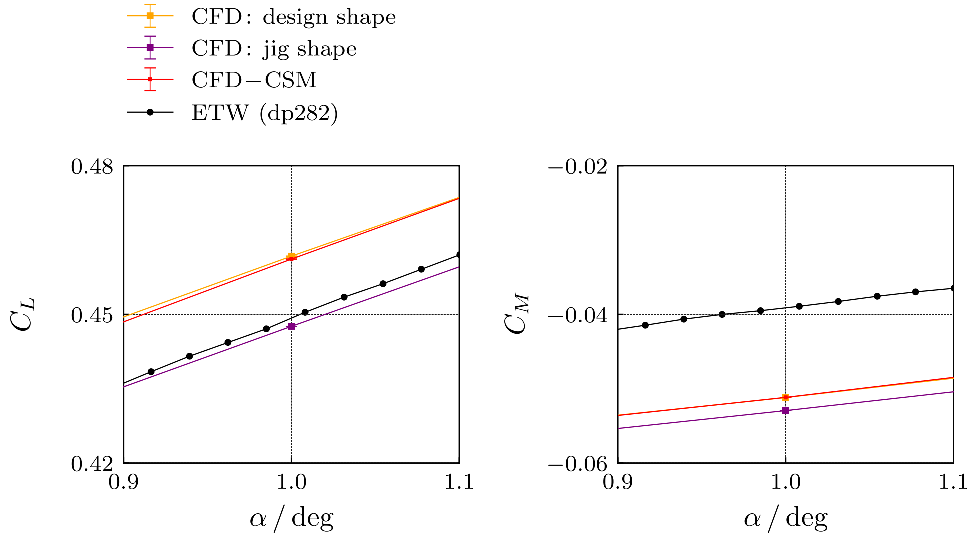

Fig. 9 Detail view of turbulent lift and moment coefficients without QCR and SSTRC

Fig. 10 Fully turbulent experimental and computational pressure coefficient distributions from CFD–CSM computations with and without QCR and SSTRC

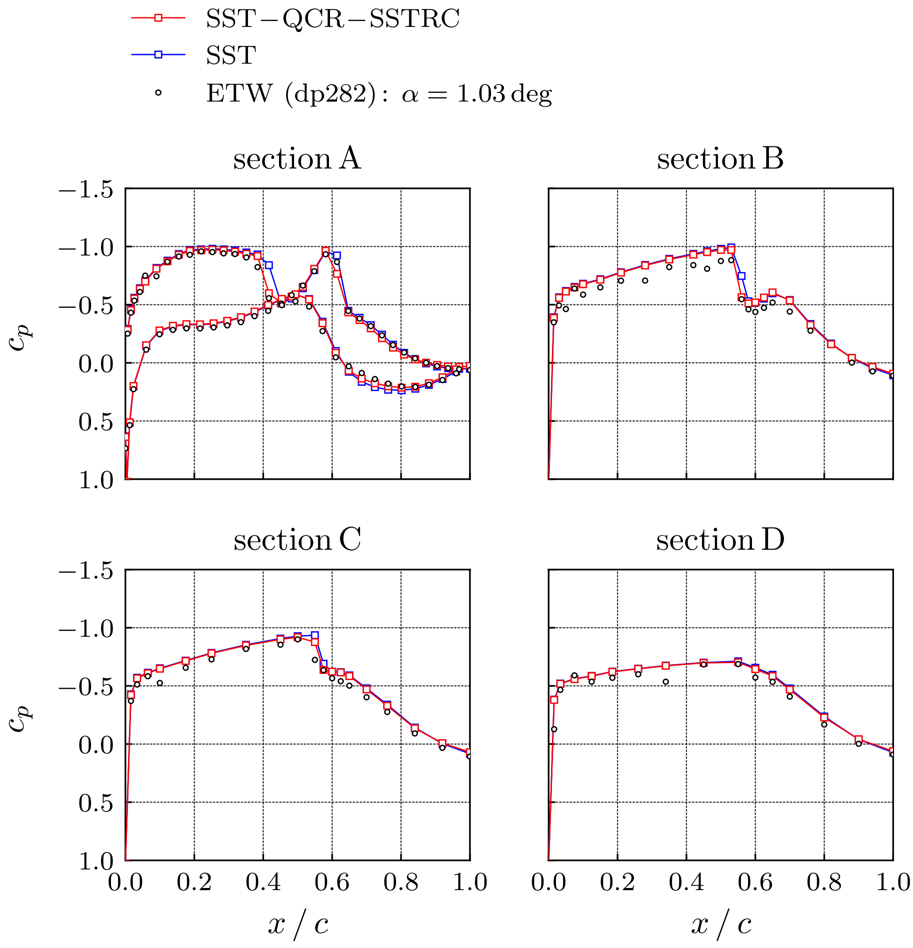

Fig. 11 Experimental and computational bending and twist distributions for fully turbulent flows with and without QCR and SSTRC

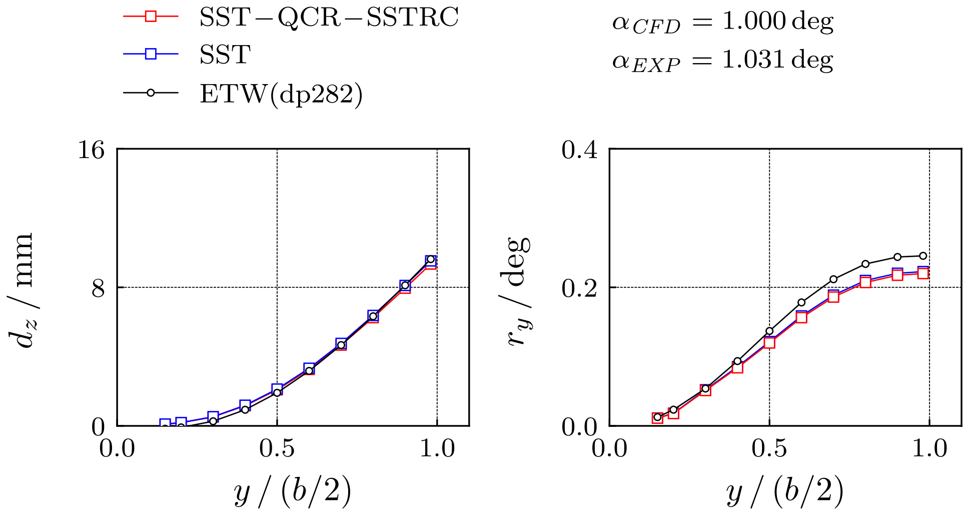

is defined in the same way as for the fully turbulent computations. A numerical transition tripping is applied on the fuselage and the lower wing surface at the experimental tripping locations. All computations are performed with the QCR and SSTRC modification.

Figure 12 shows the lift and moment coefficients in the full angle of attack range measured in the experiment. CFD computations are performed for $-3° \leq \alpha \leq 3°$. As not all computations converge to a steady solution, error bars are included to show the maximum deviation from the mean.

Fig. 12 Transitional lift and moment coefficient curves in the full experimental angle of attack range

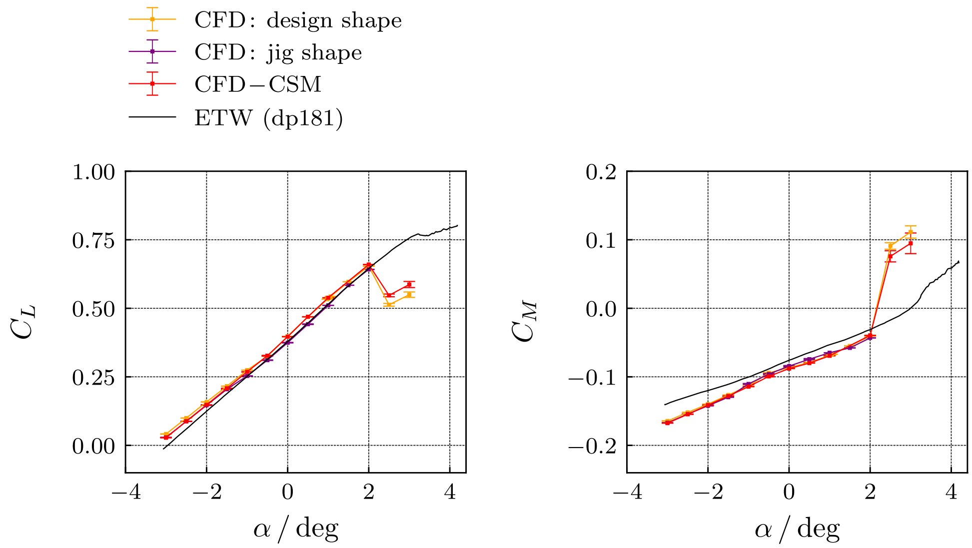

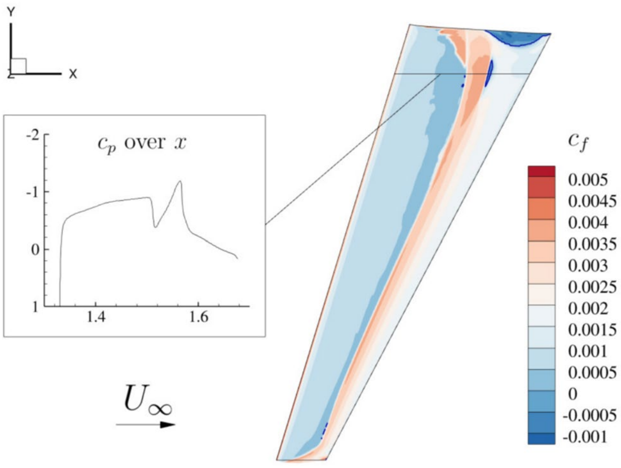

Fig. 13 Skin friction coefficient distribution on the upper wing surface of the jig shape and local pressure coefficient distribution at $\alpha = 0.5°$. The blue line marks $c_f = 0$

The solver terminates without any solution (i.e., NaN) for the rigid jig shape computations for angles of attack $\alpha > 2°$ for the given numerical settings. Changing to an upwind scheme for the discretization of the mean flow equations might give a more stable solver behavior for these angles of attack. However, the non-linear lift curve region is not part of this study and further computations will be postponed to later investigations.

The unsteadiness hindering convergence at higher angles of attack is again caused by the combined effect of a corner separation at the wing–fuselage intersection and an inboard shock on the wing upper surface with shock-induced separation in combination with the transition onset. Figure 13 shows this complex flow condition on the upper surface of the jig shape through the skin friction coefficient and a local pressure coefficient distribution: at the wing–fuselage intersection, transition occurs upstream of the first shock. The second shock downstream is directly followed by a large corner separation. Further outboard, transition occurs at the first shock, which is directly followed by a second, stronger shock causing the turbulent boundary layer to separate.

The corner separation grows strongly in size for angles of attack $\alpha > 2°$ causing a sudden decrease in lift. This effect persists despite a variation in numerical parameters and grid resolution. Although TSP images, the static pressure distribution in section A, and the lift and moment curves indicate a corner separation in the experiment for large angles of attack, the CFD computations are clearly not able to reproduce the right flow conditions for angles of attack $\alpha > 2°$.

Prior CFD computations based on the TAU transition module predicted transition due to crossflow instabilities for negative angles of attack [4]. The TSP images for angles of attack $\alpha < -1°$ show an increasingly strong jig-saw pattern at the transition location characteristic for crossflow transition, confirming the predictions by Helm et al. [4]. Although the DLR γ transition model allows for the prediction of crossflow transition, the present investigation is only focused on cases without crossflow transition to exclude the additional increase in model complexity. In consequence, the transition behavior and aerodynamic coefficients for angles of attack $\alpha < -1°$ are not captured (cf. Fig. 12).

It should be noted that the DLR γ transition model and similar models are usually not calibrated and validated to be used in combination with modifications like QCR and SSTRC. For flow conditions presented in this study, no direct effect on the transition behavior is found by applying QCR and SSTRC. Figure 14 shows the experimental and numerical pressure coefficient distributions computed for the rigid design shape at $\alpha = 1°$ with and without QCR and SSTRC. The CFD data are only evaluated at the

Fig. 14 Transitional rigid design shape computations with and without QCR and SSTRC

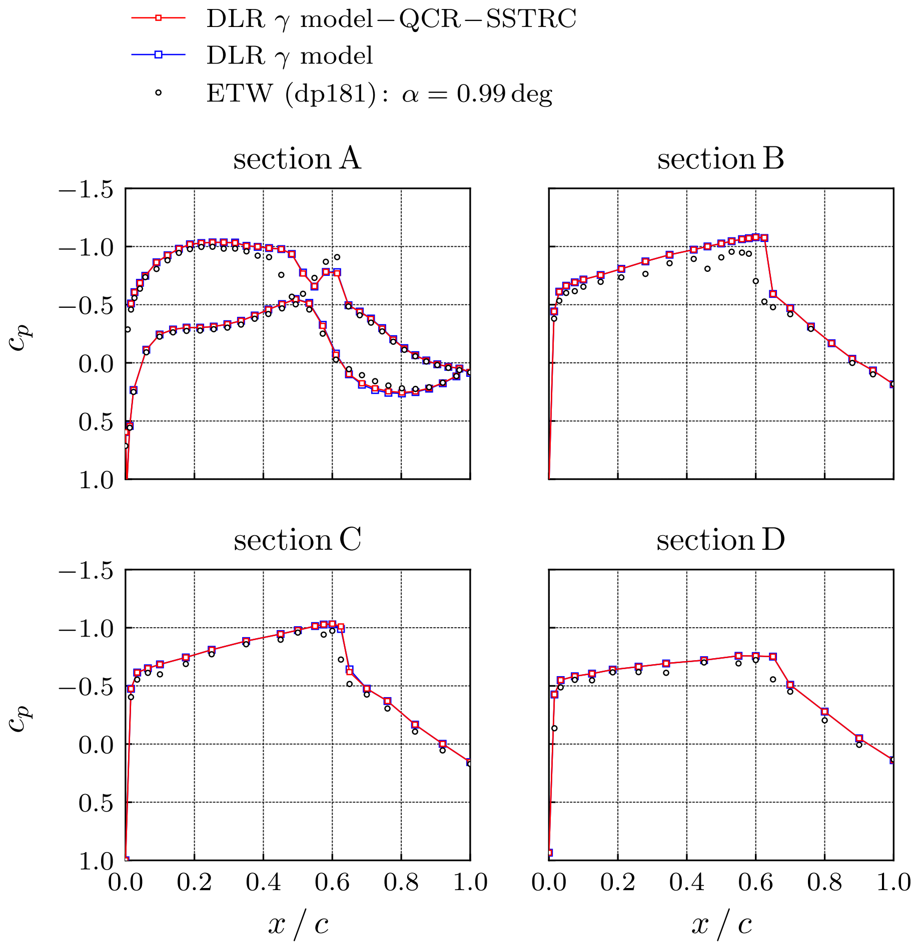

experimental pressure sensor locations. There is only a minor effect on the aft loading on the lower surface. This effect is consistent with the fully turbulent computations shown in Fig. 10. The shock location in section A is not affected.

The further analysis is focused on $\alpha = 1°$ with lift coefficients close to the design point shown in Fig. 15. The CFD computations for the design shape and the coupled CFD–CSM computations show a significant deviation from the experimental data. To explain this deviation, a coupled

Fig. 15 Experimental and computed lift and moment coefficient curves at the design lift coefficient

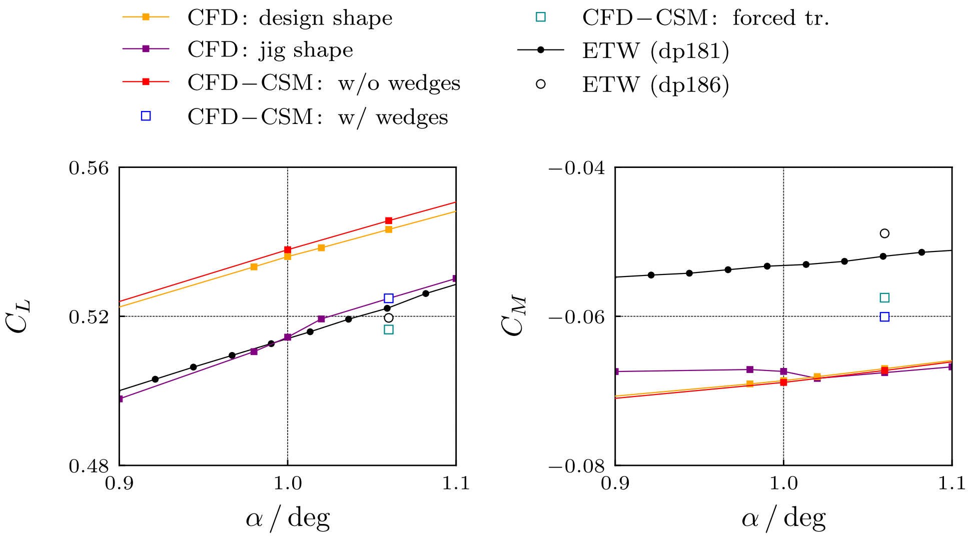

CFD–CSM computation is performed for $\alpha = 1.06°$ with turbulent wedges as measured in the experiment for this angle of attack (dataset dp186). At the wedge apices read from the TSP image, as shown in Fig. 16a, the transition onset is forced by the turbulent wedge method. Between these locations, the transition onset is freely determined by the transition model. In an additional computation, transition is forced directly at the experimental transition location over the whole wing span. This is possible as the transition location predicted by the DLR γ transition model is at or downstream of the experimental transition location.

Once the turbulent wedges are included in the coupled computation, the lift coefficient is correctly predicted and the moment coefficient is in much better agreement with the experimental data. A further improvement is achieved by forcing the whole experimental transition line in the coupled computation.

Figure 16 shows the measured TSP light emission intensity (a), the skin friction coefficient distribution from the CFD–CSM computation for free transition (b), and the computation with turbulent wedges (c). Although the measured intensity shown in Fig. 16a is not calibrated to infer any quantitative information on the skin friction, the transition location and turbulent wedges are clearly visible. The computed transition location is included as a solid black line in Fig. 16a. Disregarding any turbulent wedges found in the experiment, the DLR γ transition model gives a good prediction of the transition location. Only on the most outer TSP pocket, the transition location is predicted too far downstream. As shown in Fig. 16c, the wedge angles given by the transition model are slightly larger than in the experiment and the orientation of the angle bisectors is too steep towards the leading edge.

Figures 17 and 18 show the experimental and computational pressure coefficient distributions for the rigid jig and design shape with free transition and the CFD–CSM computations with and without turbulent wedges at $\alpha = 1.06°$, respectively. Again, the CFD data are only evaluated at the experimental pressure sensor locations. The main difference between design and jig shape is found for section A. The double shock system and the pressure recovery downstream are not reproduced by the rigid computations. The coupled computation without turbulent wedges shown in Fig. 18 results in a shock position too far downstream in all measurement sections. The results are strongly improved by the turbulent wedge model. As seen in Fig. 16c, the pressure sensors are directly affected by turbulent wedges and the numerical wedge model gives an improved description of the actual boundary-layer flow and the resulting pressure distribution.

Figure 19 shows the experimental and computed bending and twist distributions. The computations are performed at $\alpha = 1.06°$ with free transition without turbulent wedges and with the turbulent wedges measured in the experiment (dp186). As SPT deformation measurements and TSP measurements are not performed at the same time, the data from experimental run dp181 are used for comparison. Both computations give a good representation of the model deformations. The effect of the turbulent wedges is not significant, although the effect is pronounced for the aerodynamic coefficients and the pressure distributions.

4 Conclusion

This article presents a computational analysis of a wind tunnel test of a forward swept laminar wing configuration in the LuFo VI/2 project ULTIMATE. A key goal of the project is the validation of the predictive capabilities of the intermittency-based DLR γ transition model in transonic high Reynolds number flows. The investigation presented here includes rigid jig and design shape computations as well as coupled CFD–CSM computations to account for model deformation. The computations show that the correlation-based transition model is able to predict the transition location in the linear lift curve region correctly. In addition, a numerical method

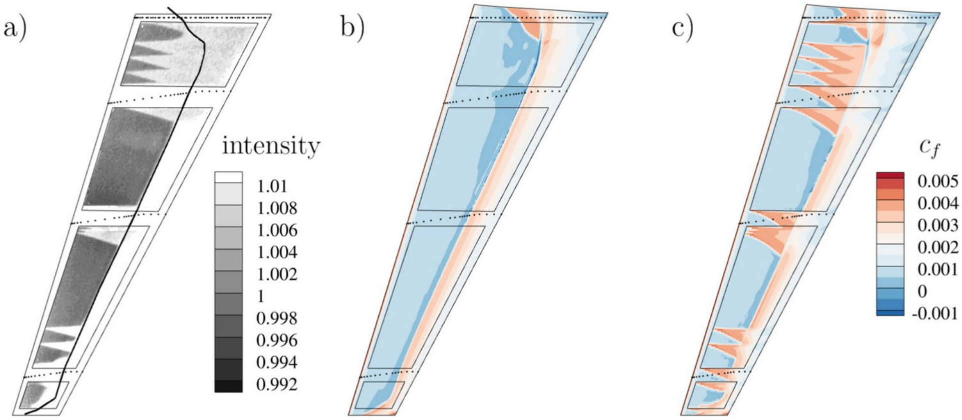

Fig. 16 **a** Measured TSP light emission intensity with transition location from CFD–CSM computation, **b** CFD–CSM skin friction coefficient distribution for free transition, **c** CFD–CSM skin friction coefficient distribution with turbulent wedges

Fig. 17 Experimental and computational pressure coefficient distributions for the rigid jig and design shape computations with free transition at $\alpha = 1.06°$

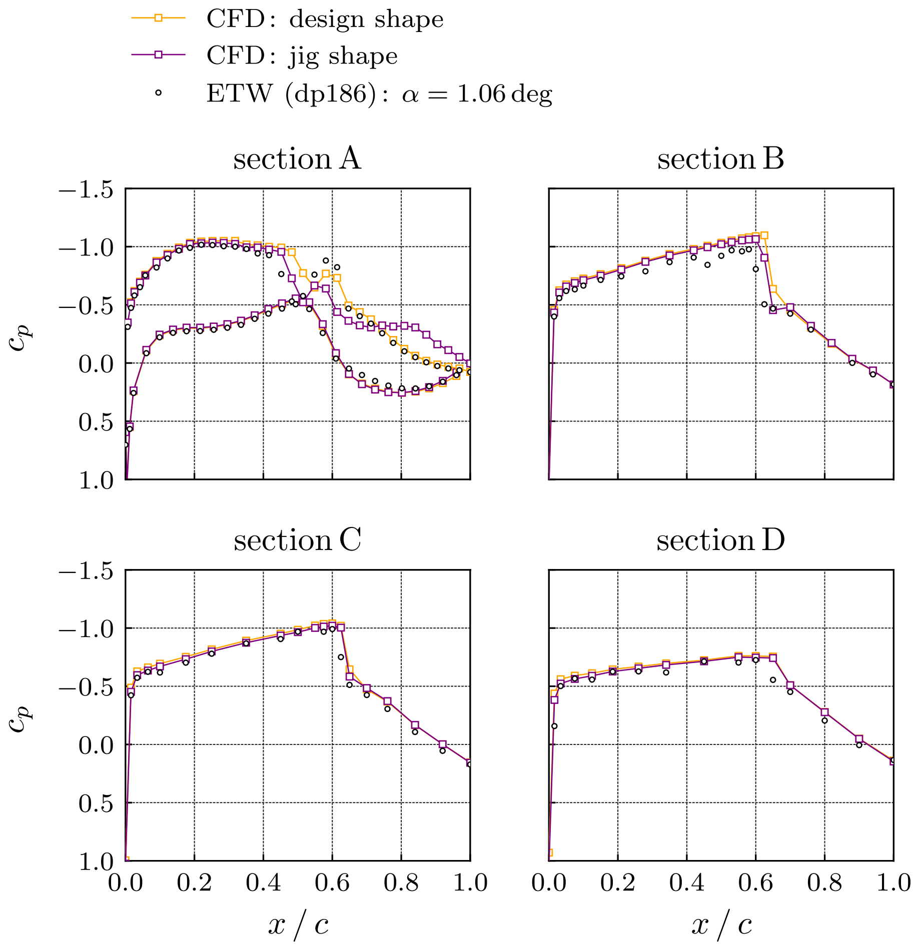

to introduce turbulent wedges in the laminar boundary-layer flow is used to improve the agreement between computed results and experimental data. The turbulent wedge model allows a more precise computation of the aerodynamic coefficients and the pressure distributions measured in the wind tunnel.

The application of a turbulent wedge model in combination with a transition model will not only foster the understanding and interpretation of wind tunnel data but will also help to develop a more precise understanding of future laminar aircraft. Turbulent wedges will occur for any laminar configuration due to inevitable surface imperfections or contaminations during operation. A turbulent wedge model can give a more robust assessment of the actual benefits of a laminar configuration by including some random turbulent wedge distribution for certain parts of the flight mission.

Future work will address specific details, e.g., grid effects, number of structural modes, and turbulence level, and will include the assessment of measurement points in the full experimental angle of attack range. This includes crossflow transition cases at low angles of attack and flow conditions in the non-linear lift curve region at high angles of attack. These steady computations are a precursor for an unsteady numerical and experimental investigation of the NLF-ECOWING-FSW with a pitching wing.

Fig. 18 Experimental and computational pressure coefficient distributions from CFD–CSM computations with and without turbulent wedges at $\alpha = 1.06°$

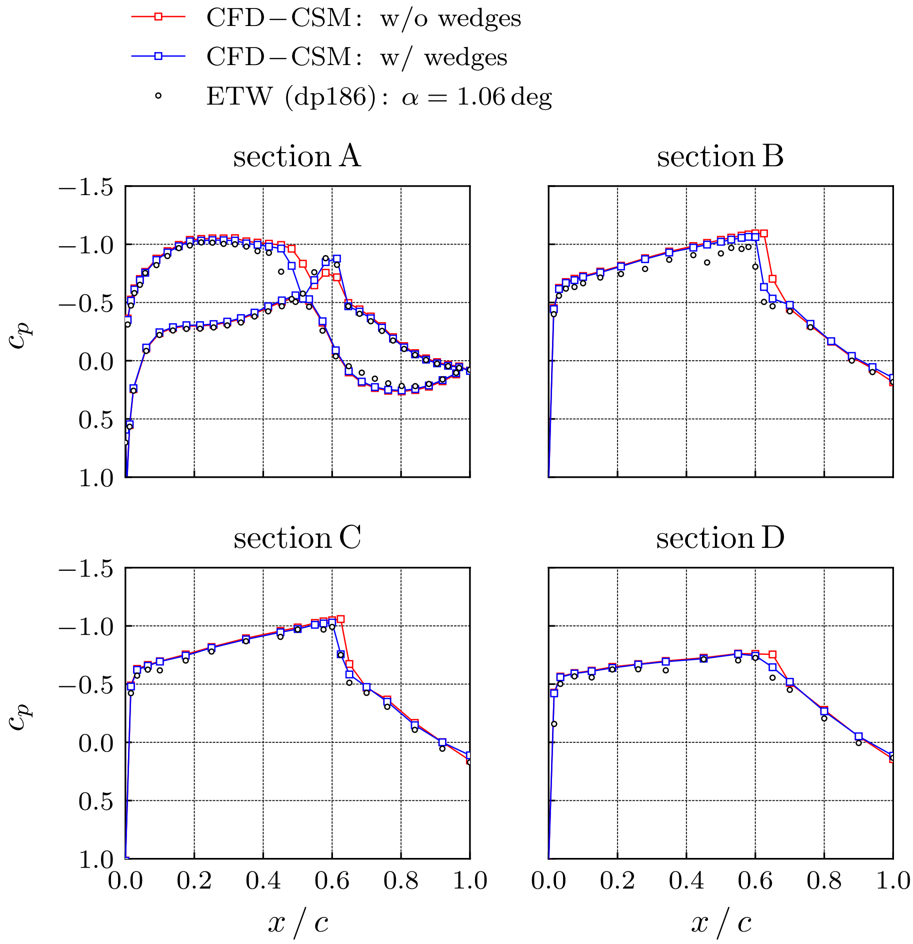

Fig. 19 Experimental and computed bending and twist distributions for transitional flows with and without turbulent wedges

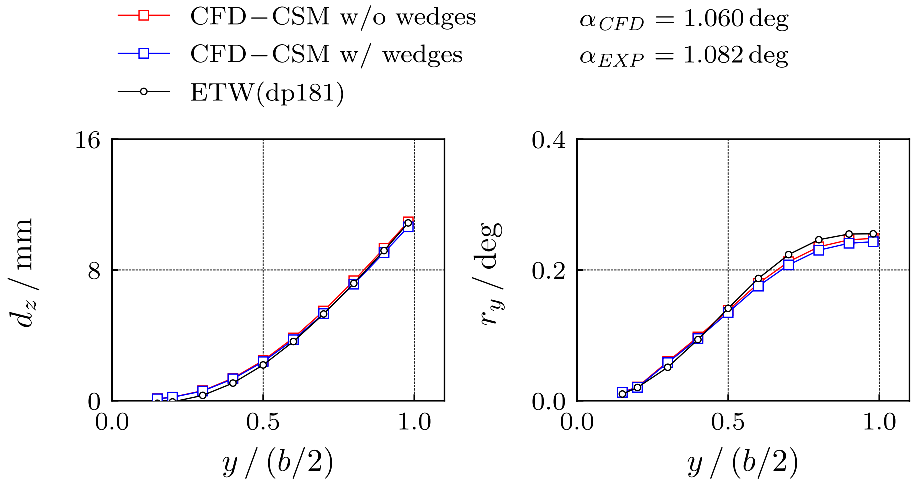

Author contributions M.F. wrote the main manuscript, conducted the computations, and prepared the figures. C.K. provided the CFD–CSM coupling environment. All authors reviewed the manuscript.

Funding Open Access funding enabled and organized by Projekt DEAL. This work is supported by the Federal Ministry for Economic Affairs and Climate Action (BMWK) on the basis of a decision by the German Bundestag.

Data availability Certain data of this study are available from the corresponding author upon reasonable request.

Declarations

Conflict of interest The authors declare that they have no conflict of interest.

References

1. Schulz, M.: LuFo VI-2 ULTIMATE forward-swept wing half model performance test in ETW. Test Report E 9018 TR 214, ETW (2022)
2. Seitz, A., Hübner, A., Risse, K.: The DLR TuLam project: design of a short and medium range transport aircraft with forward swept NLF wing. CEAS Aeronaut. J. **11**, 449–459 (2020). https://doi.org/10.1007/s13272-019-00421-1
3. Davies, K.-M., Fehrs, M., Helm, S.: Static aeroelasticity of a wind tunnel model with a forward-swept laminar wing. In: 19th International Forum on Aeroelasticity and Structural Dynamics, IFASD, IFASD-2022-168. Madrid, 13–17 June (2022)
4. Helm, S., Davies, K., Fehrs, M.: First comparison of CFD simulation and wind tunnel test of the forward-swept natural laminar flow model NLF-ECOWING-FSW. In: Dillmann, A., Heller, G., Krämer, E., Wagner, C., Weiss, J. (eds.) New Results in Numerical and Experimental Fluid Mechanics XIV, pp. 425–434. Springer, Cham (2024). https://doi.org/10.1007/978-3-031-40482-5_40
5. Krumbein, A., Krimmelbein, N., Schrauf, G.: Automatic transition prediction in hybrid flow solver, part 1: methodology and sensitivities. J. Aircr. **46**(4), 1176–1190 (2009). https://doi.org/10.2514/1.39736
6. Krumbein, A., Krimmelbein, N., Schrauf, G.: Automatic transition prediction in hybrid flow solver, part 2: practical application. J. Aircr. **46**(4), 1191–1199 (2009). https://doi.org/10.2514/1.39738
7. van Ingen, J.L.: A suggested semi-empirical method for the calculation of the boundary layer transition region. Rapport VTH-74, TU Delft (1956)
8. Smith, A.M.O., Gamberoni, N.: Transition, pressure gradient and stability theory. ES 26388, Douglas Aircraft Co. (1956)
9. van Hinsberg, N., Henne, U., Weiss, A., Risius, S., Klein, C.: Temperature sensitive paint measurement in ETW for investigation of the natural laminar flow on an innovative forward swept wing. In: Dt. Luft- und Raumfahrt Kongress, DLRK, Stuttgart (2023)
10. Helm, S., Fehrs, M., Kaiser, C., Krimmelbein, N., Krumbein, A.: Numerical simulation of the common research model with natural laminar flow. J. Aircr. **60**(2), 449–460 (2023). https://doi.org/10.2514/1.C036889
11. François, D.G., Krumbein, A., Krimmelbein, N., Grabe, C.: Simplified stability-based transition transport modeling for unstructured computational fluid dynamics. J. Aircr. **60**(6), 1773–1784 (2023). https://doi.org/10.2514/1.C037163
12. Fehrs, M.: Turbulent wedge modeling in intermittency-based transition models at high Reynolds numbers. Aerosp. Sci. Technol. **153**, 109413 (2024). https://doi.org/10.1016/j.ast.2024.109413
13. Schwamborn, D., Gerhold, T., Heinrich, R.: The DLR TAU-Code: Recent applications in research and industry. In: ECCOMAS 2006, Delft (2006)
14. Menter, F.R., Kuntz, M., Langtry, R.: Ten years of industrial experience with the SST turbulence model. In: Hanjalić, K., Nagano, Y., Tummers, M. (eds.) Turbulence, Heat and Mass Transfer 4, pp. 625–632. Begell House Inc., Redding (2003)
15. Spalart, P.R.: Strategies for turbulence modelling and simulations. Int. J. Heat Fluid Flow **21**(3), 252–263 (2000). https://doi.org/10.1016/S0142-727X(00)00007-2
16. Smirnov, P.E., Menter, F.R.: Sensitization of the SST turbulence model to rotation and curvature by applying the Spalart–Shur correction term. Turbo Expo: Power for Land, Sea, and Air, vol. 6: Turbomachinery, Parts A, B, and C, pp. 2305–2314 (2008). https://doi.org/10.1115/GT2008-50480
17. Swanson, R.C., Turkel, E.: On central-difference and upwind schemes. J. Comput. Phys. **101**(2), 292–306 (1992). https://doi.org/10.1016/0021-9991(92)90007-L
18. Dwight, R.: Efficiency improvements of RANS-based analysis and optimization using implicit and adjoint methods on unstructured grids. PhD thesis, University of Manchester, Manchester (2006)
19. Fehrs, M.: Boundary layer transition in external aerodynamics and dynamic aeroelastic stability. PhD thesis, TU Braunschweig, Braunschweig (2018)
20. François, D.G., Krumbein, A.: On the coupling of a gamma-based transition transport model to the negative Spalart–Allmaras turbulence model. In: 56th 3AF International Conference on Applied Aerodynamics. 3AF, Toulouse (2022)
21. CentaurSoft: CENTAUR Grid Generator. https://www.centaursoft.com. Accessed 24 October 2023 (2023)
22. Ansys® Mechanical Enterprise: Mechanical User's Guide, Release 2022 R2. ANSYS, Inc., Canonsburg (2022)
23. Ansys® DesignModeler: DesignModeler User's Guide, Release 2022 R2. ANSYS, Inc., Canonsburg (2022)
24. Ansys® Mechanical Enterprise: Meshing User's Guide, Release 2022 R2. ANSYS, Inc., Canonsburg (2022)
25. Reimer, L.: The FlowSimulator—a software framework for CFD-related multidisciplinary simulations. In: European NAFEMS Conference: Computational Fluid Dynamics (CFD)—Beyond the Solve. München, 2–3 December (2015)
26. Broyden, C.G.: A class of methods for solving nonlinear simultaneous equations. Math. Comput. **19**(92), 577–593 (1965). https://doi.org/10.2307/2003941
27. Duchon, J.: Splines minimizing rotation-invariant semi-norms in Sobolev spaces. In: Schempp, W., Zeller, K. (eds.) Constructive Theory of Functions of Several Variables, pp. 85–100. Springer, Berlin (1977). https://doi.org/10.1007/BFb0086566
28. Barnewitz, H., Stickan, B.: Improved mesh deformation. In: Eisfeld, B., Barnewitz, H., Fritz, W., Thiele, F. (eds.) Management and Minimisation of Uncertainties and Errors in Numerical Aerodynamics: Results of the German Collaborative Project MUNA, pp. 219–243. Springer, Berlin (2013). https://doi.org/10.1007/978-3-642-36185-2_9
29. Klein, C., Henne, U., Deisuke, Y., Ondruss, V., Beifuss, U., Hensch, A.-K., Quest, J.: Application of carbon nanotubes and temperature sensitive paint for the detection of boundary layer transition under cryogenic conditions (invited). In: 55th AIAA Aerospace Sciences Meeting. AIAA, Grapevine (2017). https://doi.org/10.2514/6.2017-0336